

## Applying petrophysical models to radar travel time and electrical resistivity tomograms: Resolution-dependent limitations

Frederick D. Day-Lewis<sup>1</sup>

U.S. Geological Survey, Office of Ground Water, Branch of Geophysics, Storrs, Connecticut, USA

Kamini Singha<sup>2</sup>

Department of Geosciences, Pennsylvania State University, University Park, Pennsylvania, USA

Andrew M. Binley

Department of Environmental Science, Lancaster University, Lancaster, UK

Received 8 December 2004; revised 2 May 2005; accepted 19 May 2005; published 24 August 2005.

[1] Geophysical imaging has traditionally provided qualitative information about geologic structure; however, there is increasing interest in using petrophysical models to convert tomograms to quantitative estimates of hydrogeologic, mechanical, or geochemical parameters of interest (e.g., permeability, porosity, water content, and salinity). Unfortunately, petrophysical estimation based on tomograms is complicated by limited and variable image resolution, which depends on (1) measurement physics (e.g., electrical conduction or electromagnetic wave propagation), (2) parameterization and regularization, (3) measurement error, and (4) spatial variability. We present a framework to predict how core-scale relations between geophysical properties and hydrologic parameters are altered by the inversion, which produces smoothly varying pixel-scale estimates. We refer to this loss of information as “correlation loss.” Our approach upscales the core-scale relation to the pixel scale using the model resolution matrix from the inversion, random field averaging, and spatial statistics of the geophysical property. Synthetic examples evaluate the utility of radar travel time tomography (RTT) and electrical-resistivity tomography (ERT) for estimating water content. This work provides (1) a framework to assess tomograms for geologic parameter estimation and (2) insights into the different patterns of correlation loss for ERT and RTT. Whereas ERT generally performs better near boreholes, RTT performs better in the interwell region. Application of petrophysical models to the tomograms in our examples would yield misleading estimates of water content. Although the examples presented illustrate the problem of correlation loss in the context of near-surface geophysical imaging, our results have clear implications for quantitative analysis of tomograms for diverse geoscience applications.

**Citation:** Day-Lewis, F. D., K. Singha, and A. M. Binley (2005), Applying petrophysical models to radar travel time and electrical resistivity tomograms: Resolution-dependent limitations, *J. Geophys. Res.*, 110, B08206, doi:10.1029/2004JB003569.

### 1. Introduction

[2] Geophysical tomography (seismic, electromagnetic, electrical, and radar) is commonly used in petroleum engineering, global seismology, and hydrogeologic studies. Tomograms provide valuable, qualitative information about geologic, aquifer and reservoir structure and processes, as reported by abundant examples in the literature. Contrasts in electromagnetic (EM), electrical, or seismic properties provide information about lithology, rock fractures, depth to bedrock, depth to water table, and other structures and

properties of geologic relevance. In the environmental and petroleum fields, tomograms are used increasingly for more quantitative estimation of hydraulic properties. Petrophysical formulas are used to convert geophysical images into two-dimensional (2-D) cross sections or three-dimensional (3-D) volumes of quantities such as saturation, concentration, porosity, or permeability [e.g., Hubbard *et al.*, 2001; Slater *et al.*, 2002; Berthold *et al.*, 2004]. In some cases, site-specific conversions are used [e.g., Alumbaugh *et al.*, 2002], whereas in others, general petrophysical relations such as Archie's law [Archie, 1942] are applied [e.g., Slater *et al.*, 2002]. To account for uncertain and nonunique relations between geophysical properties and the hydrologic parameter of interest, some have considered conditional simulation, Bayesian, and co-kriging frameworks [e.g., McKenna and Poeter, 1995; Cassiani *et al.*, 1998; Hubbard *et al.*, 2001]. In some studies, models of statistical spatial

<sup>1</sup>Formerly at Bucknell University, Lewisburg, Pennsylvania, USA.

<sup>2</sup>Formerly at Department of Geological and Environmental Sciences, Stanford University, Stanford, California, USA.

structure (i.e., the variogram or covariance) have been inferred from tomograms. Such work implicitly assumes that tomographic estimates approximate point-scale measurements. Unfortunately, for many practical field situations tomographic estimates should be viewed as weighted local averages because tomograms bear the imprint of prior information and regularization criteria, survey geometry, measurement physics, and measurement error.

[3] Although qualitative insights into subsurface architecture are readily made from geophysical data, quantitative use of geophysical images to estimate values of hydrologic parameters suffers from limitations arising from imperfect and variable tomographic resolution. Geotomography tends to overpredict the extent and underpredict the magnitude of geophysical targets; moreover, the spatial structure of tomograms may only weakly reflect the true spatial structure of the subsurface. In this paper, we refer to this loss of information as “correlation loss.” This problem was recognized by *McKenna and Poeter* [1995], who noted weak correlation between tomographic estimates of seismic velocity and colocated measurements of hydraulic conductivity compared to the correlation seen for higher resolution sonic logs; they derived a correction based on regression and applied the correction uniformly over the tomogram to compensate for the correlation loss. Similarly, *Cassiani et al.* [1998] noted correlation loss between tomographic estimates of seismic velocity and hydraulic conductivity in poorly resolved regions of tomograms. In an effort to monitor tracer experiments with electrical-resistivity tomography (ERT), *Singha and Gorelick* [2005] noted the impact of regularization and inversion artifacts on the estimated spatial moments of the tracer plume. In an ERT study to monitor a fluid tracer in the vadose zone, *Binley et al.* [2002] applied locally derived petrophysical relations to convert resistivity tomograms to changes in moisture content; their analysis revealed a 50% mass balance error that was attributed to the poor sensitivity in the center of the image volume where the tracer was applied.

[4] Quantifying tomographic resolution and geophysical measurement support is a long-standing and active area of geophysical research [e.g., *Dahlen*, 2004; *Sheng and Schuster*, 2003; *Friedel*, 2003; *Alumbaugh and Newman*, 2000; *Oldenburg and Li*, 1999; *Schuster*, 1996; *Rector and Washbourne*, 1994; *Ramirez et al.*, 1993; *Menke*, 1984; *Backus and Gilbert*, 1968]. Resolution depends on the measurement physics; physical approximations in the forward model and (or) sensitivity calculation; survey design; measurement error; regularization criteria and inversion approach; and parameterization. The correlation between point-scale measurements of hydrologic and geophysical properties is commonly degraded by the inversion process, which produces images that represent blurry, blunted, and artifact-prone versions of reality.

[5] Recently, *Day-Lewis and Lane* [2004] investigated the implications of correlation loss and variable model resolution for geostatistical utilization of tomograms. Analytical methods were developed to model the correlation loss as a function of measurement physics, survey geometry, measurement error, spatial correlation structure of the subsurface, and regularization. For the simplified case of linear, ray theoretic radar tomography and linear correlation between radar slowness ( $1/\text{velocity}$ ) and the natural loga-

rithm of permeability, they derived formulas to predict (1) how the inversion process degrades the correlation between imaged geophysical properties and related hydrologic parameters, compared to point measurements, (2) how the variance of the estimated geophysical parameter compares to the variance of the true property, and (3) how the inversion alters the spatial covariance of the estimated parameter. Using synthetic examples for radar travel time tomography (RTT), they demonstrated that tomograms of qualitative value may hold limited quantitative utility for standard geostatistical applications.

[6] In this paper, we extend the methodology of *Day-Lewis and Lane* [2004] to consider nonlinear tomographic inversion and nonlinear petrophysical relations; furthermore, we compare correlation loss, variance reduction, and tomogram spatial structure for RTT and ERT. In the present treatment of radar tomography, we use a more physically based forward model and sensitivity calculation that accounts for refraction and finite frequency limitations on measurement sensitivity and tomographic resolution. The goals of the present study are (1) to raise awareness of the limitations of geophysical data, (2) to provide a framework to improve survey design and assess tomograms for hydrologic estimation, and (3) to develop insights into the different patterns of correlation loss for electrical resistivity and radar tomography. Although the examples used to illustrate our approach are based on near-surface radar and electrical tomography to characterize variations in water content, our approach is applicable to other forms of geotomography, and our results have implications for quantitative use of tomograms across geoscience subdisciplines.

## 2. Approach

[7] Similar in concept to medical CT scan imaging technology, geotomography yields two- or three-dimensional images, i.e., tomograms, of the spatially variable physical properties of the subsurface. Geotomography has provided high-resolution information for understanding deep earth structure [e.g., *Aki et al.*, 1977; *Zandt*, 1981] and near-surface aquifer heterogeneity [*Hyndman and Gorelick*, 1996; *Hubbard et al.*, 2001; *McKenna and Poeter*, 1995]; improved management of petroleum reservoirs [*Bregman et al.*, 1989]; monitoring natural hydrologic processes [*Park*, 1998; *Binley et al.*, 2001] and engineered remediation [*Lane et al.*, 2005; *Slater and Binley*, 2003]; and interpretation of hydrologic field experiments [*Day-Lewis et al.*, 2003, 2004; *Singha and Gorelick*, 2005]. Here, we consider two tomographic modalities: radar travel time tomography (RTT) and electrical-resistivity tomography (ERT).

### 2.1. Forward Modeling and Sensitivity Calculation

#### 2.1.1. Radar Travel Time Tomography

[8] In cross-hole RTT, travel times of EM waves are measured between transmitter and receiver antennas that are placed at many different locations in two boreholes. Travel times are inverted for spatially variable radar slowness ( $1/\text{velocity}$ ), which is related to dielectric permittivity and therefore moisture content, porosity, and lithology. Commonly, forward models for RTT use either (1) the straight-ray approximation, which neglects EM wave refraction and is inappropriate in the presence of significant

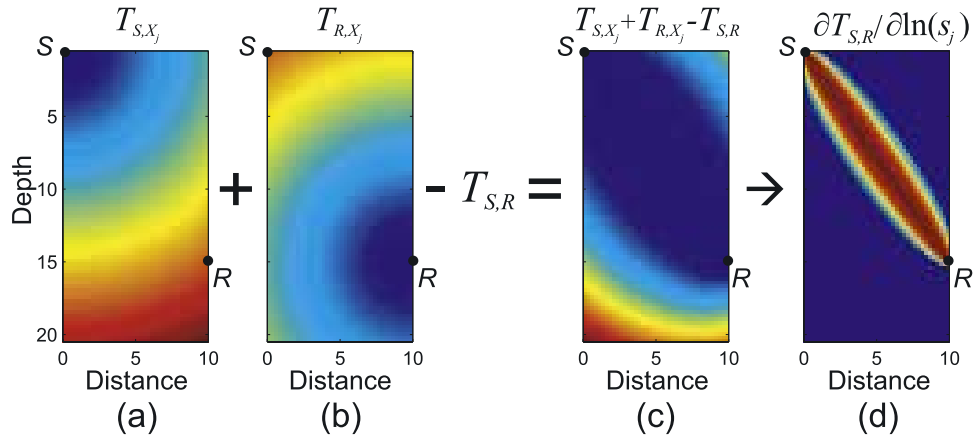


**Figure 1.** Schematic diagram illustrating fat ray sensitivity calculation: (a) cross-sectional image of calculated travel times,  $T_{S,X_j}$ , from source location,  $S$ , to centers of all pixels,  $j$ ; (b) cross-sectional image of calculated travel times,  $T_{R,X_j}$ , from receiver location,  $R$ , to centers of all pixels,  $j$ ; (c) cross-sectional image of the quantity  $|T_{S,X_j} + T_{R,X_j} - T_{S,R}|$ ; (d) cross-sectional image of the sensitivity of the travel time between  $S$  and  $R$ , to the natural logarithm of pixel slowness values. Sensitivity decreases linearly from the infinite frequency ray path axis to the edge of the Fresnel volume. The width of the “fat ray” is a function of the dominant frequency.

(>10%) velocity contrasts [e.g., Peterson, 2001], (2) ray-tracing algorithms [e.g., Cerveny, 1984], or (3) numerical solution of the eikonal equation [Vidale, 1988, 1990]:

$$(\nabla T)^2 = \frac{1}{v^2}, \quad (1)$$

where  $T$  is the time of first arrival and  $v$  is the EM wave velocity.

[9] Conventional ray theoretic approaches to calculate RTT sensitivity do not account for resolution limitations arising from the underlying measurement physics; that is, the same Jacobian would be obtained regardless of the dominant frequency. To achieve a fair comparison of correlation loss in RTT and ERT, we seek to account for the effect of wave behavior on resolution. To this end, we adopt a Fresnel volume approach to the sensitivity calculation for inversion of travel time data [e.g., Watanabe et al., 1999; Husen and Kissling, 2001]. Fresnel volume or “fat ray” tomography is an appealing compromise between efficient ray theoretic approaches and computationally burdensome full waveform inversion.

[10] In ray theoretic tomography, travel times are modeled as line integral measurements along infinitesimal width ray paths; in contrast, Fresnel volume tomography treats travel times as volume integral measurements, where the support volume is approximated by the first Fresnel zone [Vasco et al., 1995]. For a pixilated grid, the Fresnel zone is defined as the region containing all pixels,  $j$ , such that

$$\Delta t_j = |T_{S,X_j} + T_{R,X_j} - T_{S,R}| \leq \frac{1}{2f}, \quad (2)$$

where

$T_{S,X_j}$  travel time for the fastest path between the source and the center of pixel  $j$ ;

$T_{R,X_j}$  travel time for the fastest path between the receiver and the center of pixel  $j$ ;

$T_{S,R}$  travel time for the fastest path between the source and receiver;

$f$  dominant frequency of the EM waves.

We calculate first-arrival times,  $T_{S,X_j}$ ,  $T_{R,X_j}$ , and  $T_{S,R}$ , numerically using a finite difference eikonal solver.

[11] To calculate the Jacobian matrix for use in the inversion procedure, a protocol is needed to distribute measurement sensitivity over the Fresnel volume. We follow an approach proposed by Watanabe et al. [1999], in which more weight is attributed to pixels nearer the axis of the Fresnel volume, i.e., the infinite frequency ray path, where  $\Delta t$  is equal to zero. Alternative wave theoretic approaches to sensitivity calculation are possible [Spetzler and Snieder, 2004]. The weight,  $\omega_j$ , decreases linearly from the axis to zero at the edge of the Fresnel volume (Figure 1):

$$\omega_j = \begin{cases} 1 - 2f\Delta t_j, & 0 \leq \Delta t_j \leq 1/2f \\ 0, & \Delta t_j \geq 1/2f \end{cases}. \quad (3)$$

The sensitivity of a calculated travel time,  $t$ , to the slowness in pixel  $j$ ,  $s_j$ , is calculated as

$$\frac{\partial t}{\partial s_j} = \frac{\omega_j}{\sum_{k=1}^N \omega_k} T_{S,R}. \quad (4)$$

It should be noted that the fat ray modification of ray theory does not account for scale-dependent scattering. In practice, discrepancies between the physics incorporated into the forward model and the physics underlying the measurements will result in additional error and lower resolution.

### 2.1.2. ERT

[12] Cross-hole ERT is used to estimate the distribution of electrical resistivity in the subsurface by establishing an electrical gradient between two source electrodes and measuring the resultant potential distribution at two or more

receiving electrodes [Binley and Kemna, 2005]. This procedure is repeated for many combinations of source and receiver electrode positions, and usually involves the acquisition of many hundreds or thousands of four-electrode measurements. The ERT forward problem is described by the Poisson equation

$$-\nabla \cdot \rho^{-1} \nabla \phi = I \delta(x - x_s, y - y_s, z - z_s), \quad (5)$$

subject, in this work, to Neumann (no current flow) boundary conditions, where

- $\rho$  electrical resistivity;
- $\phi$  electrical potential;
- $I$  electrical current source;
- $\delta$  Dirac delta function;
- $x, y, z$  spatial position vectors;
- $x_s, y_s, z_s$  spatial coordinates of the current source.

[13] For the problems here, we consider only 2-D variation in resistivity (in the plane of the boreholes), but still account for 3-D electrical current flow. Consequently, equation (5) can be modified to

$$-\nabla_{xz} \cdot \rho^{-1} \nabla_{xz} \phi^* + \frac{\lambda^2}{\rho} \phi^* = I \delta(x - x_s, z - z_s), \quad (6)$$

where  $\lambda$  is the Fourier transform variable corresponding to the strike direction  $y$  and  $\phi^*$  is the potential in the Fourier domain. Adopting this approach, an inverse Fourier transformation must be applied to the solution of equation (6) to recover potentials  $\phi$  [see, e.g., LaBrecque et al., 1996].

[14] Numerical solution of (6) is performed using a finite element model with a 2-D mesh of linear-quadrilateral elements; other numerical methods, including finite differences, could be used. Inverse modeling requires numerical calculation of the Jacobian of simulated ERT measurements with respect to model resistivities at each iteration. This matrix may be computed using the principle of reciprocity [Geselowitz, 1971] as detailed, for example, by Kemna [2000].

## 2.2. Inversion Approach

[15] We seek, to the extent practical, to use similar inversion approaches and regularization for ERT and RTT to facilitate insights into the influence of measurement physics on resolution and correlation loss. The nonlinear inversion seeks to identify the vector of model parameters that minimize an objective function,  $F$ , consisting of two terms: (1) the least squares, weighted misfit between observed and predicted measurements, and (2) a smoothness-based measure of solution complexity based on a second-derivative spatial filter:

$$F = (\mathbf{d} - g(\hat{\mathbf{m}}))^T \mathbf{C}_D^{-1} (\mathbf{d} - g(\hat{\mathbf{m}})) + \alpha \hat{\mathbf{m}}^T \mathbf{D}^T \mathbf{D} \hat{\mathbf{m}}, \quad (7)$$

where

- $\mathbf{d}$  vector of measurements, i.e., radar travel time or electrical resistance;

- $g(\ )$  forward model for first arrival time (1) or electric potential (6);
- $\hat{\mathbf{m}}$  vector of parameter estimates;
- $\mathbf{C}_D$  covariance matrix of measurement errors;
- $\alpha$  weight that determines the trade-off between data misfit and regularization;
- $\mathbf{D}$  model-weighting regularization matrix (i.e., a discretized second-derivative filter for the reference example).

The model parameters are updated in an iterative fashion by repeated solution of a linear system of equations for  $\Delta \hat{\mathbf{m}}$  at successive iterations:

$$[\mathbf{J}^T \mathbf{C}_D^{-1} \mathbf{J} + \alpha \mathbf{D}^T \mathbf{D}] \Delta \hat{\mathbf{m}} = \mathbf{J}^T \mathbf{C}_D^{-1} (\mathbf{d} - g(\hat{\mathbf{m}}_{k-1})) - \alpha \mathbf{D}^T \mathbf{D} \hat{\mathbf{m}}_{k-1} \quad (8a)$$

$$\hat{\mathbf{m}}_k = \hat{\mathbf{m}}_{k-1} + \Delta \hat{\mathbf{m}}, \quad (8b)$$

where

- $\mathbf{J}$  Jacobian matrix, with elements  $J_{ij} = \partial \hat{d}_i / \partial \hat{m}_j$ ;
- $\hat{d}_i$  calculated value of measurement  $i$ ;
- $\hat{\mathbf{m}}_k$  vector of parameter estimates after updating in iteration  $k$ ; and
- $\Delta \hat{\mathbf{m}}$  vector of parameter updates for iteration  $k$ .

At each iteration of the inversion, a new Jacobian is calculated around the last set of parameter estimates. After obtaining the new estimate by solution of (8), a line search is performed to identify the  $\alpha$  value that results in the expected root-mean-square (RMS) prediction error given the model of measurement errors. If such a value cannot be found, then the  $\alpha$  that gives the lowest RMS error is taken, and the algorithm proceeds to the next iteration. The inversion continues until (1) the RMS error reaches the target RMS error, (2) the reduction in RMS error between successive iterations is less than a specified tolerance, or (3) a maximum number of iterations is reached. This approach is commonly referred to as an Occam inversion.

[16] Following standard practice for ERT [Tripp et al., 1984; Daily and Owen, 1991; LaBrecque et al., 1996] and travel time tomography [Tarantola, 2004, pp.123–125], our estimation parameters are the natural logarithm of pixel resistivity,  $\ln(\rho)$ , and the natural logarithm of pixel slowness divided by the mean slowness,  $\ln(s/\mu_s)$ , respectively. Estimation of log parameters has two desirable traits. First, it ensures that the inversion never yields negative, unphysical estimates of slowness or resistivity. Second, it yields more reliable results in situations where the geophysical parameter varies by orders of magnitude, which is common in ERT. For the case of travel time tomography, inversion of  $\ln(s/\mu_s)$  amounts to estimating deviations of  $\ln(s)$  from the mean of  $\ln(s)$ .

## 2.3. Resolution of Tomograms

[17] The resolution of tomograms depends on (1) the measurement physics, for example electrical conduction or electromagnetic wave propagation, (2) the survey geometry, (3) the parameterization and regularization used for inversion, and (4) measurement error. For the radar problem,

there exist several approaches for evaluating the resolution of tomograms. For seismic, and by analogy radar tomography, *Dahlen* [2004] recently derived formulas to relate 3-D images of estimated slowness to the true slowness field assuming complete source-receiver coverage and linearized ray theory; however, this and other diffraction-tomography approaches to resolution are not capable of accounting for measurement error, inadequate ray path coverage, or the effect of regularization. For straightforward and quantitative comparison of resolution for the RTT and ERT problems, we instead use the concept of the model resolution matrix [e.g., *Menke*, 1984; *Ramirez et al.*, 1993; *Alumbaugh and Newman*, 2000; *Day-Lewis and Lane*, 2004].

[18] Conceptually, the model resolution matrix is the lens or filter through which the inversion *sees* the study region. For a linear inverse problem,

$$\begin{aligned}\hat{\mathbf{m}} &= [\mathbf{J}^T \mathbf{C}_D^{-1} \mathbf{J} + \alpha \mathbf{D}^T \mathbf{D}]^{-1} \mathbf{J}^T \mathbf{C}_D^{-1} \mathbf{d} \\ &\approx [\mathbf{J}^T \mathbf{C}_D^{-1} \mathbf{J} + \alpha \mathbf{D}^T \mathbf{D}]^{-1} \mathbf{J}^T \mathbf{C}_D^{-1} \mathbf{J} \mathbf{m}_{true},\end{aligned}\quad (9)$$

the model resolution matrix,  $\mathbf{R}$ , is defined as

$$\mathbf{R} = [\mathbf{J}^T \mathbf{C}_D^{-1} \mathbf{J} + \alpha \mathbf{D}^T \mathbf{D}]^{-1} \mathbf{J}^T \mathbf{C}_D^{-1} \mathbf{J}, \quad (10)$$

and thus

$$\hat{\mathbf{m}} \approx \mathbf{R} \mathbf{m}_{true}. \quad (11)$$

[19] For linear problems, where  $\mathbf{J}$  is independent of  $\mathbf{m}_{true}$ ,  $\mathbf{R}$  can be calculated prior to data collection. Given a model of measurement errors, the model resolution matrix can be calculated using (10) and used as a tool to assess and refine hypothetical survey designs and regularization criteria. In interpreting inversion results,  $\mathbf{R}$  is useful for identifying likely inversion artifacts [*Day-Lewis et al.*, 2002]. For nonlinear problems,  $\mathbf{R}$  can be approximated using the  $\mathbf{J}$  and  $\alpha$  from the last iteration of the inversion [e.g., *Alumbaugh and Newman*, 2000]. In strongly nonlinear problems, resolution is a strong function of the model parameters, and thus  $\mathbf{R}$  cannot be calculated reliably prior to conducting the survey and inverting the data.

#### 2.4. Modeling Correlation Loss

[20] *Day-Lewis and Lane* [2004] recently presented an approach to evaluate the resolution-dependent utility of tomograms for geostatistics by combining the definition of the model resolution matrix [e.g., *Alumbaugh and Newman*, 2000] and random field averaging (RFA) [*Vanmarcke*, 1983]. They considered examples for linear, straight ray radar tomography and a linearly correlated hydrologic parameter of interest (i.e., log permeability,  $\ln(k)$ ). Here, we extend their methodology to consider nonlinear tomographic inversion and nonlinear petrophysical relations; furthermore, we compare patterns of correlation loss and variance reduction for ERT and RTT. For the radar problem, we consider a forward model and sensitivity calculation that accounts more fully for wave behavior, including refraction and finite frequency limitations on resolution.

[21] The approach of *Day-Lewis and Lane* [2004] assumes (1) that the geophysical parameter and hydrologic property of interest are normally distributed, (2) both

properties share the same covariance structure, and (3) both properties are second-order stationary, i.e., the mean and variance are spatially uniform and the covariance between two points depends only on the separation between them. Under these assumptions, and given the statistics of the true radar slowness and  $\ln(k)$  fields, *Day-Lewis and Lane* [2004] predicted the variance reduction of the pixel-scale tomographic estimate compared to the point-scale property; the correlation loss between the tomographic estimate and a second property, compared to the point-scale correlation; and the spatial covariance between pixel estimates. Similar results could be achieved through brute force generation of a large number of realizations, forward modeling of tomographic data, tomographic inversion, and comparison of the resulting tomograms with the original realizations [*Singha and Moysey*, 2004]. We now provide a brief summary of the approach to assessing the geostatistical value of tomograms for the linear problem; we then extend the approach to nonlinear petrophysical relations and inversion.

[22] According to (11), tomographic estimates can be interpreted as weighted averages of the true values of the imaged property, where the weights are described by the rows of  $\mathbf{R}$ :

$$\hat{m}_i \approx \sum_{j=1}^n R_{ij} m_j^{true}. \quad (12)$$

The statistical properties of weighted averages of random functions, such as the average described by (12), can be predicted using random field averaging [*Vanmarcke*, 1983]; thus tomographic estimates can be interpreted as upscaled, weighted averages of point-scale properties.

[23] Consider linear, weighted averages  $\bar{X}_1$  and  $\bar{X}_2$  of a homogeneous random function,  $X$ , with covariance structure  $\sigma_{X_i, X_j}$ :

$$\bar{X}_1 = \sum_{i=1}^N a_i X_i \quad \bar{X}_2 = \sum_{j=1}^N b_j X_j, \quad (13)$$

where  $a$  and  $b$  are weights. The covariance between weighted averages is

$$\sigma_{\bar{X}_1, \bar{X}_2} = \sum_{i=1}^N \sum_{j=1}^N a_i b_j \sigma_{X_i, X_j}, \quad (14)$$

and variance of the weighted average  $\bar{X}_1$  is found by substituting  $\bar{X}_2 = \bar{X}_1$ :

$$\sigma_{\bar{X}_1}^2 = \sum_{i=1}^N \sum_{j=1}^N a_i a_j \sigma_{X_i, X_j}. \quad (15)$$

For the case of a linear relation between the point-scale property  $X$  and a second property,  $Z$ , with covariance  $\sigma_{X_i, Z_j}$ , the covariance between  $\bar{X}_1$  and  $\bar{Z}_j$  is merely:

$$\sigma_{\bar{X}_1, \bar{Z}_j} = \sum_{i=1}^N a_i \sigma_{X_i, Z_j}. \quad (16)$$

Assuming, for the moment, a linear relation between  $X$  and  $Z$ , a Markov type 2 approximation [*Journel*, 1999] predicts

the cross covariance between  $X$  at location  $i$  and  $Z$  at location  $j$ :

$$\sigma_{X_i, Z_j} \approx r_{X,Z} \sqrt{\sigma_Z^2 / \sigma_X^2} \sigma_{X_i, X_j}, \quad (17)$$

where  $r_{X,Z}$  is the correlation coefficient between colocated point-scale  $X$  and  $Z$ .

[24] Modeling estimated pixel values as a weighted average using (12), applying (14 and 16) to the results, and modeling the cross covariance between the geophysical parameter,  $m$ , and the hydrologic parameter of interest,  $p$ , with (16), we find

$$\hat{\sigma}_{\hat{m}_i}^2 = \sum_{j=1}^N \sum_{k=1}^N R_{ij} R_{ik} \sigma_{m_j, m_k}, \quad (18)$$

$$\hat{\sigma}_{\hat{m}_i, \hat{m}_k} = \sum_{j=1}^N \sum_{l=1}^N R_{ij} R_{kl} \sigma_{m_j, m_l}, \quad (19)$$

$$\hat{r}_{\hat{m}_i, p_i} = \frac{\sigma_{\hat{m}_i, p_i}}{\sqrt{\sigma_{\hat{m}_i}^2 \sigma_{p_i}^2}} \approx r_{m,p} \hat{r}_{m_i, \hat{m}_i} = r_{m,p} \sum_{j=1}^N R_{ij} \sigma_{m_i, m_j} / \sqrt{\sigma_m^2 \hat{\sigma}_{\hat{m}_i}^2}. \quad (20)$$

Equations (18)–(20) provide insights into (1) how the ensemble variance of the estimated geophysical parameter,  $\hat{\sigma}_{\hat{m}_i}^2$ , compares to  $\sigma_m^2$ , which is assumed stationary; (2) whether the spatial covariance of the estimated geophysical parameter,  $\hat{\sigma}_{\hat{m}_i, \hat{m}_k}$ , reflects true structure or merely the applied regularization; and (3) how the correlation coefficient between the estimated geophysical parameter and the colocated hydrologic parameter,  $\hat{r}_{\hat{m}_i, p_i}$ , varies spatially and is diminished by inversion compared to the true, point-scale correlation,  $r_{m,p}$ . The variance predicted by (18) should not be confused with estimation error; rather it indicates the inversion's tendency to diminish variations in the geophysical parameter. For an ensemble of realizations of  $m$  with variance  $\sigma_m^2$ , (18) predicts the variance of the pixel estimates of  $m_i$  taken across a corresponding ensemble of tomograms.

[25] For simplicity, *Day-Lewis and Lane* [2004] assumed a linear petrophysical relation between the geophysical property and hydrologic parameter of interest. Here, we consider nonlinear petrophysical relations, and thus cannot rely on the Markov approximation for the cross covariance or quantify the apparent petrophysical relation between colocated tomographic estimates and hydrologic parameters using the correlation coefficient,  $\hat{r}_{\hat{m}_i, p_i}$  (20); rather, for each pixel, we transform the geostatistically simulated  $\ln(s)$  or  $\ln(\rho)$  to water content using the Topp equation [*Topp et al.*, 1980] or Archie's law [*Archie*, 1942], respectively. Our approach is general and alternative petrophysical relations are possible; moreover, uncertainty in the petrophysical relations could be considered by assuming different models to transform the simulated geophysical property to water content.

### 2.5. Pixel-Specific Apparent Petrophysical Relations

[26] It is clear that correlation loss varies spatially according to local resolution, as indicated by equations (18)–(20)

and demonstrated in work by *Day-Lewis and Lane* [2004]; thus the apparent petrophysical relation between, for example, estimated radar velocity and true water content, will be pixel-specific. In this section, we develop an approach to predict pixel-specific apparent petrophysical relations within a probabilistic framework. For an ensemble of realization/tomogram pairs, a specific pixel would have, under our assumptions, a Gaussian distribution of the natural logarithm of the geophysical estimation parameter (i.e.,  $\ln(s)$  or  $\ln(\rho)$ ) with mean and variance  $\mu_m$  and  $\sigma_m^2$ . Looking across realizations, when pixel  $i$  takes on a particular value of  $m_i$ , the resulting tomographic estimate,  $\hat{m}_i$ , will follow a distribution that can be modeled as Gaussian with a conditional mean predicted using a regression developed from (18)–(20):

$$E[\hat{m}_i | m_i] = \hat{r}_{\hat{m}_i, m_i} \frac{\sigma_{\hat{m}_i}}{\sigma_m} (m_i - \mu_m) + \mu_m, \quad (21)$$

and a conditional standard deviation equal to

$$\hat{\sigma}_{\hat{m}_i | m_i} = \hat{\sigma}_{\hat{m}_i} \sqrt{1 - \hat{r}_{\hat{m}_i, m_i}^2}. \quad (22)$$

For each pixel, we seek to construct the Gaussian probability distribution function (PDF) of the geophysical estimate,  $\hat{m}_i$ , that would result from the PDF of the true values of the geophysical parameter,  $m_i$  and (for the study here) water content,  $\theta$ . For a range of values of  $m_i$  extending from 3 standard deviations below the mean to 3 standard deviations above, we build the PDF defined by equations (21)–(22) and the bivariate Gaussian PDF function between  $m_i$  and  $\hat{m}_i$ :

$$f_{\hat{m}_i, m_i} = \frac{1}{2\pi\sigma_{m_i}\hat{\sigma}_{\hat{m}_i}} \exp\left\{-\frac{(m_i - \mu_{m_i})}{2\sigma_{m_i}^2} - \frac{(\hat{m}_i - E[\hat{m}_i | m_i])}{2\hat{\sigma}_{\hat{m}_i | m_i}^2}\right\}. \quad (23)$$

Although  $f_{\hat{m}_i, m_i}$  is useful, we are more interested in  $f_{\hat{m}_i, \theta}$ , the PDF between the geophysical estimate and the parameter of interest. To transform the  $m_i$  axis of the PDF to  $\theta_i$  involves a conversion using the core-scale petrophysical relation (introduced in the following section) and a rescaling of the PDF to account for the change in the property units and range; additional details of this procedure are provided in Appendix A. Comparison of  $f_{\hat{m}_i, \theta}$  for different pixels offers insight into the reliability of quantitative estimates of geologic properties made by application of petrophysical models to tomograms.

[27] Figure 2 provides a schematic outline of the approach to developing pixel-specific apparent petrophysical relations. It should be noted that the approach assumes  $\mathbf{R}$  is not a strong function of the true field of the geophysical parameter; the applicability of the results for one slowness or resistivity field to others depends on the nonlinearity of the problem.

### 3. Examples

[28] We consider examples in which cross-hole RTT and ERT are used to image contrasts in volumetric water content (volume of water divided by the total volume), which manifest as variations in resistivity and radar slowness,

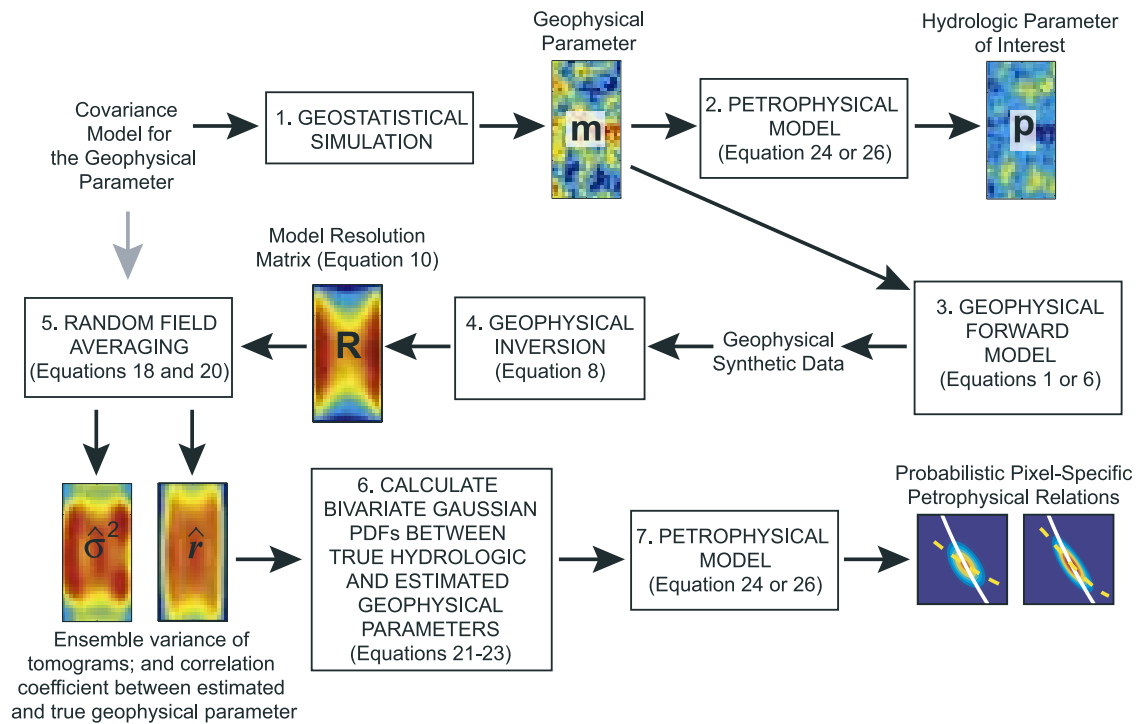


**Figure 2.** Schematic diagram illustrating the calculation of the approach. Starting from an assumed covariance describing the spatial structure of the geophysical parameter, a realization is generated (step 1) and converted using the petrophysical model to the hydrologic parameter of interest (step 2); synthetic geophysical data are calculated (step 3); the data are inverted and the model resolution matrix calculated (step 4); random field averaging is used to upscale the spatial covariance based on the model resolution matrix and calculate (1) the ensemble variance of the estimated geophysical parameter and (2) the correlation coefficient between the estimated and true geophysical parameters (step 5); bivariate probability distribution functions between the true and estimated geophysical parameter are calculated (step 6) and transformed using the petrophysical model (step 7) to yield pixel-specific petrophysical relations.

respectively. Realizations of  $\ln(s)$  and  $\ln(\rho)$  were generated using the sequential Gaussian simulation program SGSIM [Deutsch and Journel, 1998]. The SGSIM algorithm generates random fields (realizations) based on (1) a spatially uniform mean, (2) a spatially uniform variance, and (3) a model of spatial variability between points described by a variogram, which is related to the spatial covariance. The algorithm can produce realizations conditional to point data and other information, including volume averages.

[29] We assume  $\ln(s)$  and  $\ln(\rho)$  are second-order stationary, have a correlation structure described by a spherical variogram [e.g., Deutsch and Journel, 1998, p. 25], and are multivariate normal, i.e., the joint probability density function between values at multiple locations is Gaussian. In order to achieve a fair comparison of RTT and ERT, and

also to rigorously satisfy the assumptions of our approach (sections 2.4–2.5), we simulate random fields of the geophysical estimation parameters rather than random fields of water content. Structurally identical random fields of  $\ln(s)$  and  $\ln(\rho)$  are used for RTT and ERT examples. The mean and variance of the geophysical estimation parameters (Table 1) were selected such that the water content fields would cover the same range for ERT and RTT examples. For the base case, a correlation length of 4 m is assumed; in other examples, we examine the effect of changing the correlation length and variance. A porosity of 0.25 is assumed; for the RTT and ERT base cases, water content varies from 0.08 to 0.20, for an equivalent saturation (volume of water divided by the volume of voids) range of 0.32 to 0.8.

**Table 1.** Examples for Radar Travel Time Tomography

Radar Examples	Correlation Length, m	Standard Deviation of $\ln(s)$	Regularization	Maximum Ray Path Angle, deg	Frequency, MHz
1, base case	4	0.047	second derivative	63.4	200
2, effect of correlation length	2	0.047	second derivative	63.4	200
3, effect of variation in $\ln(s)$	4	0.094	second derivative	63.4	200
4, effect of regularization	4	0.047	smallness	63.4	200
5, effect of angular coverage	4	0.047	second derivative	45	200
6, effect of wavelength	4	0.047	second derivative	63.4	100

[30] For both ERT and RTT, the interwell region extends 10 m horizontally and 20 m vertically. Identical realizations are used for both ERT and RTT; however, the forward models for the ERT and RTT have different measurement physics and therefore different discretization and boundary requirements. The ERT forward model requires a grid much larger than the interwell region to minimize the effect of model boundaries; conversely, the eikonal solver requires less padding around the interwell region but finer discretization between the wells. To accommodate both ERT and RTT considerations, the geostatistical simulation grid extends 269 m horizontally and 150 m vertically, and is discretized into square pixels, 0.5 m on a side. The RTT inversion is performed on a  $24 \times 44$  subgrid of the geostatistical simulation grid, centered around the interwell region. For the eikonal solver, the slowness grid is further discretized into square pixels 0.25 m on a side. For ERT, the inversion grid extends over the full geostatistical simulation grid, with expanding grid spacing outside the interwell region. In the outer grid, geostatistically simulated  $\ln(\rho)$  values are upscaled to variable size grid cells according to the arithmetic mean of  $\ln(\rho)$  values (i.e., the geometric mean of  $\rho$  values) for component cells.

[31] To account for the role of measurement error in correlation loss, small but realistic zero mean, uncorrelated normal random errors are added to the simulated measurements. For ERT, the standard error was assumed equal to 3% of each measurement value. For RTT, the standard error was taken as one sample period, assumed to be 0.5 ns for all measurements; this is consistent with observations by *Alumbaugh et al.* [2002].

### 3.1. Radar Examples

[32] For the base case scenario, geostatistical realizations of  $\ln(s)$  [ $\mu\text{s}/\text{m}$ ] are generated assuming a mean of  $-4.68$  and standard deviation of  $0.047$ . The empirical Topp equation [Topp *et al.*, 1980] is used to relate volumetric water content,  $\theta$ , and radar slowness:

$$\theta = -5.3 \times 10^{-2} + 2.9 \times 10^{-2} \varepsilon_r - 5.5 \times 10^{-4} \varepsilon_r^2 + 4.3 \times 10^{-6} \varepsilon_r^3, \quad (24)$$

where  $\varepsilon_r$  is the relative dielectric permittivity (dimensionless). The Topp equation is based on time domain reflectometry measurements made on a variety of soils at different saturation levels. It should be noted that other petrophysical models, such as the complex refractive index model (CRIM) [Birchak *et al.*, 1974] could be considered. Radar slowness is related to dielectric permittivity by

$$s = \sqrt{\varepsilon_r}/c, \quad (25)$$

where  $c$  is the electromagnetic wave velocity in air. Realizations of  $\ln(s)$  are transformed to water content using the petrophysical relation (24) and (25).

[33] A series of examples investigates the effects of correlation length and variation of  $\ln(s)$ , survey geometry, wavelength, and regularization correlation loss (Table 1). For each  $\ln(s)$  field, we solve (1) for the first arrival times that would be measured in the field for 1681 source-receiver pairs, given two wells, 10 m apart, with 40 antenna positions in each well. The antenna locations are separated

in depth by 0.5 m, and span 20 m in depth. The simulated first-arrival travel times are inverted using (8), assuming the same standard errors for  $C_D$  that were used to add error to the simulated measurements. The inversion continues until a target RMS, which is also based on the assumed error model, is achieved. Following the final iteration, the model resolution matrix is calculated using (10). In the presence of larger errors seen in practice, the inversion would converge at a larger value of  $\alpha$ , resulting in a smoother tomogram, poorer resolution, and greater correlation loss; hence the results presented here should be viewed as best case scenarios.

#### 3.1.1. Example 1: Base Case

[34] Results for the RTT base case scenario are shown in Figure 3. In general, the radar slowness tomogram for the base case scenario (Figure 3d, example 1) captures the gross structure of the true slowness field (Figure 3b, example 1). The larger high- and low-valued slowness anomalies are recovered, although their extents are overestimated, their magnitudes underestimated, and their boundaries blurred. Examination of the diagonal of the model resolution matrix (Figure 3c, example 1) indicates that resolution is high in the middle of the interwell region and low near the boreholes and in the top-middle and bottom-middle of the tomogram; this pattern holds true for the variance of tomographic estimates and the correlation coefficient between estimated and true  $\ln(s)$ . Where the variance (Figure 3e, example 1) is lower, tomographic estimates fluctuate less from the mean value, provide less information about true  $\ln(s)$ , and are stronger functions of regularization. Where the correlation coefficient between estimated and true  $\ln(s)$  (Figure 3f, example 1) is lower, tomographic estimates are weakly related to the true values. The pattern of correlation loss for this example is similar to that predicted under the high-frequency straight-ray approximation [Day-Lewis and Lane, 2004]; however, the magnitude of correlation loss is less. Whereas Day-Lewis and Lane [2004] considered a cross-well aperture (defined as horizontal-to-vertical offset) of 1:1, the 2:1 aperture in this example permits better resolution of heterogeneity.

#### 3.1.2. Example 2: Effect of Decreased Correlation Length

[35] In this example, the correlation length of the true  $\ln(s)$  is 2 m, half that of the base case. In well resolved regions, the inversion successfully recovers smaller-scale anomalies, but in regions of low-resolution, target anomalies blur together. Compared to the base case, resolution is more spatially variable (Figure 3c, example 2), and the ensemble variance of estimates (Figure 3e, example 2) and correlation between estimated and true  $\ln(s)$  (Figure 3f, example 2) are poor.

#### 3.1.3. Example 3: Effect of Variation in Radar Slowness—Double Standard Deviation

[36] In this example, we assess the role of the magnitude of spatial variations in  $\ln(s)$  by considering a true  $\ln(s)$  field with double the standard deviation of the base case. Compared to the base case results, resolution varies more over the interwell region (Figure 3c, example 3). Refraction focuses ray paths into high-velocity areas, which tends to enhance resolution locally; however, fat rays are also “fatter” in high-velocity areas, which tends to degrade resolution. The latter effect is stronger in the middle of the tomogram (Figure 3d, example 3), resulting in stronger

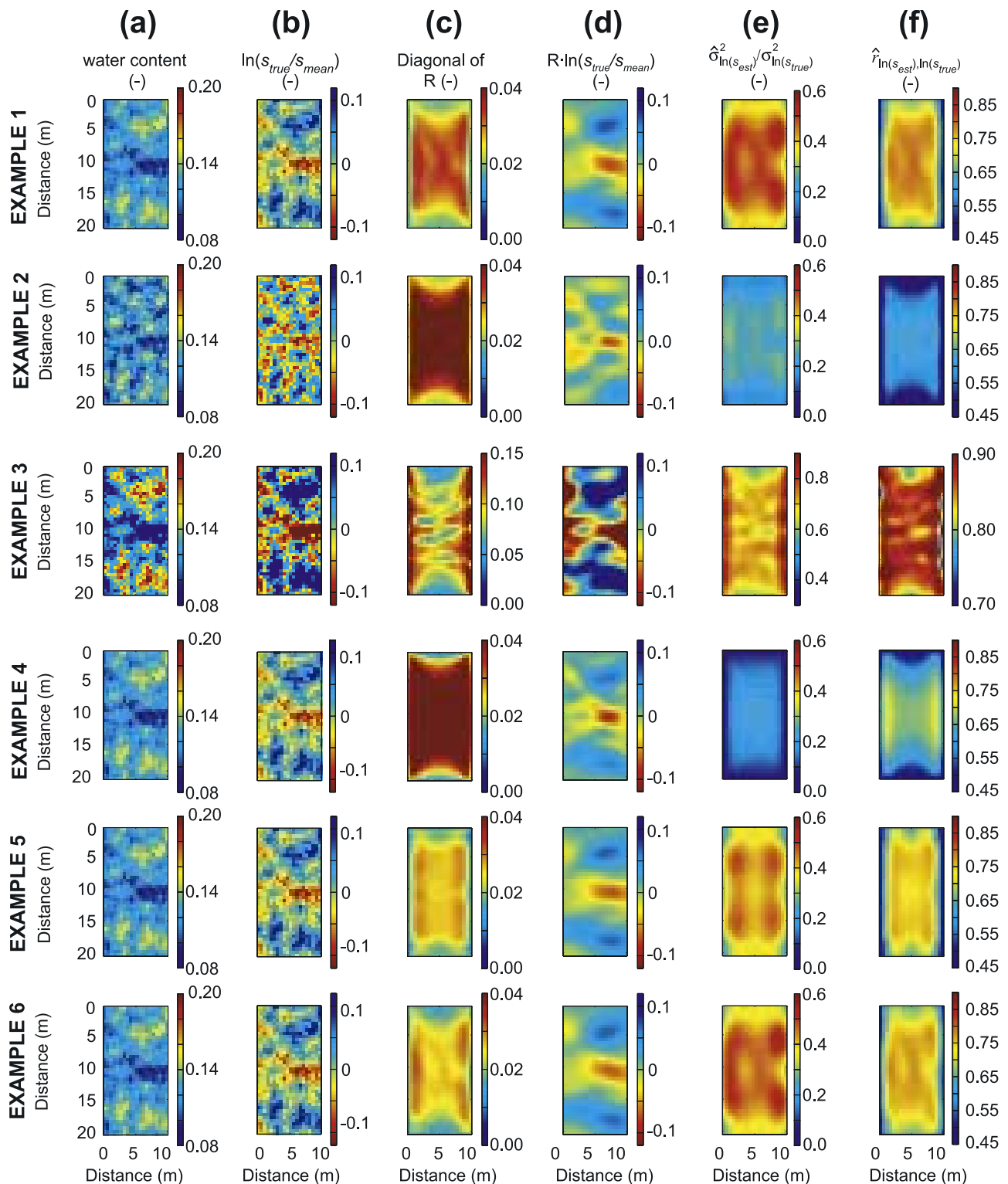


**Figure 3.** Radar travel time tomography results for examples 1–6: (1) base case; (2) decreased correlation length; (3) increased standard deviation; (4) regularization based on damping; (5) source-receiver geometry without high-angle ray paths; (6) 200 MHz dominant frequency. Cross sections of (a) water content; (b) true  $\ln(s/\mu_s)$ ; (c) diagonal of the model resolution matrix; (d) inverted tomogram of  $\ln(s/\mu_s)$ ; (e) the predicted variance of  $\ln(s/\mu_s)$  for an ensemble of tomograms, normalized by the variance of true  $\ln(s/\mu_s)$ ; and (f) the predicted correlation coefficient between true and estimated  $\ln(s/\mu_s)$ .

correlation at the boreholes and altered pattern of correlation loss compared to the base case (Figure 3f, example 3). Differences between this example and the base case arise primarily from the nonlinearity of the inverse problem; however, it should be noted that the error level, 0.5 ns, is independent of the variance, and thus the signal-to-noise ratio for this example is better than for the base case.

### 3.1.4. Example 4: Effect of Regularization

#### Criteria Smallness

[37] Smallness-based regularization, in which the model-weighting matrix  $\mathbf{D}$  is a diagonal matrix, penalizes deviations from a prior mean. Because we are estimating  $\ln(s/\mu_s)$ , which is equivalent to estimating deviations of  $\ln(s)$  from  $\ln(\mu_s)$ , the prior mean is assumed equal to zero. Qualitatively, the resulting tomogram is similar to those inverted using regularization based on a second-derivative filter. The pattern of model resolution (Figure 3c, example 4) and correlation loss (Figure 3f, example 4) resemble results for the base case; however, the ensemble variance (Figure 3e, example 4) is diminished compared to results with smoothness-based regularization, consistent with increased blunting of estimates, as expected for smallness-based regularization. These results indicate that the relation between tomographic estimates of  $\ln(s)$  and true water content will differ depending on the rather subjective choice of regularization.

### 3.1.5. Example 5: Effect of Survey Geometry—Decreased Angular Coverage

[38] Resolution is limited by the angular coverage of the interwell region. Commonly, measurements along high-angle ray paths are limited by the cross-hole geometry and poor signal-to-noise ratio for longer ray paths. In this example, we consider the subset of the data used in example 1 for which the vertical offset is less than the horizontal well offset, i.e., measurements with takeoff angles between  $-45^\circ$  and  $45^\circ$ . Loss of high-angle ray paths results in a qualitatively similar tomogram (Figure 3d, example 5), but lower resolution (Figure 3c, example 5), ensemble variance (Figure 3e, example 5) and correlation (Figure 3f, example 5), especially in the middle of the tomogram.

### 3.1.6. Example 6: Effect of Wavelength

[39] In this example, the impact of antenna frequency is investigated. We consider a dominant frequency of 100 MHz, half that of the base case. In fat ray tomography, the wavelength (a function of both frequency and local velocity) determines the “fatness” of the ray paths. With higher dominant frequency, ray path volumes grow thinner in the interwell region, enabling better resolution of small-scale structure but more variable ray density. Compared to example 1, use of a lower, 100-MHz dominant frequency results in inferior resolution, ensemble variance, and correlation (Figures 3c, 3e, and 3f, example 5), especially in the middle of the tomogram.

## 3.2. ERT Examples

[40] The pattern of correlation loss between the geophysical and hydrologic parameters is expected to be different for ERT and radar because of the difference in the governing physics of the measurements. Direct current resistivity is considered to be a steady state process defined by diffusive flow, whereas RTT measurements are based on EM wave propagation.

[41] We generated realizations of  $\ln(\rho)$  using the sequential Gaussian simulation algorithm SGSIM [Deutsch and Journel, 1998] for a  $300 \times 538$  pixel grid, assuming a spherical variogram and correlation length of 4 m. Each realization pixel is 0.5 m on a side. In contrast to the RTT forward model, the ERT model requires a grid much larger than the interwell region in order to minimize the effect of model boundaries, which are assumed to be no flow. The  $\ln(\rho)$  pixels behind the wells, extending to the distant boundaries, are upsampled using arithmetic averaging. The covariance of the  $\ln(\rho)$  field is similarly upsampled to account for the variable cell sizes. The final grid is  $52 \times 44$  pixels. The mean and standard deviation of  $\ln(\rho)$  [ohm m] realizations are 8.06 and 0.23 respectively.

[42] Using Archie’s law [Archie, 1942], the electrical resistivity realizations are converted to fluid saturation:

$$S_w = \left( \frac{\rho_f}{\rho_b} n^{-q} \right)^{\frac{1}{\kappa}}, \quad (26)$$

where

- $S_w$  fluid saturation;
- $\rho_f$  fluid electrical resistivity;
- $\rho_b$  bulk electrical resistivity;
- $n$  porosity;
- $q$  cementation exponent; and
- $\kappa$  saturation exponent.

For this work, the fluid electrical resistivity is assumed constant, and equal to 50 ohm m; the porosity is 0.25; and  $q$  and  $\kappa$  are both 2. The variations in saturation are related exactly to variations in bulk electrical resistivity through (26). Application of Archie’s law to each realization of  $\ln(\rho)$  results in saturations varying from 0.30 to 0.87, and thus water content between 0.08 and 0.22. This calculated saturation is considered the “true” saturation.

[43] For the simulated resistivity field, we forward solve (6) for the resistances that would be measured in the field for 1746 unique quadripoles, given two wells, 10 m apart, with 40 electrodes in each well. The geometry used for simulation is based on circulating dipole-dipoles, where both in-well and cross-well dipoles are considered. The electrodes are separated in depth by 0.5 m, and span from 0.5 m to 20 m below land surface. These forward model resistances are then inverted using (8) with 3% random Gaussian noise added. The stopping criterion for the ERT inversion is a target RMS error based on the added measurement error. The resolution matrix is calculated for the final iteration using (10).

[44] Measurement physics, survey design, measurement error, the spatial structure of the subsurface resistivity, and regularization all impact the resolution of the tomogram and the resultant petrophysics. Below, we discuss a series of examples (Table 2) that investigate the effect of each issue on the resultant geophysical tomograms. Results for various scenarios are compared with a “base case” example.

### 3.2.1. Example 1: Base Case

[45] In general, the electrical resistivity tomogram recovers the large-scale features of the input electrical resistivity model (Figure 4d, example 1). The final inversion is

**Table 2.** Examples for Electrical-Resistivity Tomography<sup>a</sup>

ERT Examples	Correlation Length, m	Standard Deviation of $\ln(\rho)$	Regularization	Number of Measurements	Survey Geometry
1, base case	4	0.23	second derivative	1746	mixed
2, effect of correlation length	2	0.23	second derivative	1746	mixed
3, effect of variation in $\ln(\rho)$	4	0.46	second derivative	1746	mixed
4, effect of regularization	4	0.23	second derivative, 9-pixel footprint	1746	mixed
5, effect of survey geometry	4	0.23	second derivative	672	mixed
6, effect of survey geometry	4	0.23	second derivative	672	in-well dipoles

<sup>a</sup>“Mixed” indicates both in-well and cross-well dipoles were used.

smooth—high resistivity values are underestimated and low values are overestimated; however, the larger structures are recovered reasonably well. The resolution matrix indicates that the sensitivity is higher near the electrodes, and drops off quickly toward the center of the array (Figure 4c, example 1). This variability in resolution is apparent in the tomograms; target recovery is best near the edges, where the electrodes are present, and falls toward the mean in the center of array, where data sensitivity is low. The predicted ensemble variance is consequently higher near the electrodes, and lower in the center of the plane (Figure 4e, example 1), although the ERT is never able to recover the high variability in resistivity seen in the original realization, even near the wells.

[46] The correlation between the true and estimated electrical resistivity from the ERT is also best near the wells, where the ERT resolution is high (Figure 4f, example 1). Near the electrodes there is near perfect correlation between true and estimated  $\ln(\rho)$  for these synthetic models, but this drops off away from the electrodes.

### 3.2.2. Example 2: Effect of Decreased Correlation Length

[47] The resistivity structure of the subsurface is expected to control, in part, the ability of ERT to resolve subsurface targets. In general, smaller structures are more difficult to resolve. In this example, we consider a realization generated using half the correlation length of the base case (2 m rather than 4 m (Figure 4a, example 2)). The resulting tomogram captures the smaller-scale targets near the electrodes (Figure 4d, example 2). In the middle of the tomogram, there is minimal change in resolution, variance, and correlation between estimated and true log resistivity near the wells (Figures 4c, 4e, and 4f, example 2). In these examples, the measurement physics, more than the correlation length of heterogeneity, limits resolution in the middle of the tomogram.

### 3.2.3. Example 3: Effect of Variation in Resistivity—Double Standard Deviation

[48] If we consider twice the standard deviation in resistivity of the base case, the water content varies from 0.06 to 0.27 (Figure 4a, example 3). With increased variability in resistivity, the resultant tomogram reveals more structure,

because of the true increased variability in the field (Figure 4d, example 3), but also because of the improved resolution and variance, especially near the electrodes (Figures 4c and 4e; example 3). The correlation between true and estimated  $\ln(\rho)$  also improves, especially in the center of the array (Figure 4f, example 3). The magnitude of resistivity variation has implications for the resolution of tomograms and the relation between geophysical estimates and hydrologic parameters.

### 3.2.4. Example 4: Effect of Model Filter

[49] The model filter,  $\mathbf{D}$ , used in the inversion associated with (7) affects the correlation between the geophysical parameters after inversion and also the resolution, as seen in (10). For the base case, we used a second-derivative filter, which in two dimensions is a 5-pixel roughening operator. Because inversion is solved by the minimization of (7), which includes a regularization term, the solution is ultimately the smoothest electrical resistivity field that fits the data to the specified RMS value. If we use a model filter with a wider footprint of 9 pixels, the final inversion is smoother than in the base case (Figure 4d, example 4); consequently the variance and correlation between the estimated and true electrical resistivity decrease slightly with respect to the base case (Figure 4f, example 4). Although the choice of model filter must be carefully considered when attempting to quantify the magnitude of a target, its effect on the resolution matrix may be small in certain circumstances.

### 3.2.5. Example 5: Effect of Survey Geometry—Number of Measurements

[50] The number of data collected in the field affects the resolution of the tomogram. Considering a geometry with only 672 resistance measurements, we find that we have poorer recovery of the subsurface structure in the center of the plane than for the base case, which includes 1746 quadripoles (Figure 4d, example 5). Moreover, the resolution and variance are lower in the center of plane and, because of fewer measurements than the base case, also at the wells (Figures 4c and 4e, example 5). In areas of low resolution, there will be a correspondingly poorer correlation between geophysical estimates and hydrologic parameters (Figure 4f, example 5).

**Figure 4.** ERT results for examples 1–6: (1) base case; (2) decreased correlation length; (3) increased standard deviation; (4) regularization using a smoothing filter with a larger footprint; (5) survey geometry with fewer measurements; (6) survey geometry with only in-well dipoles. Cross sections of (a) true water content, (b) true  $\rho$ ; (c) the natural logarithm of elements on the diagonal of the model resolution matrix, (d) the inverted tomogram of  $\ln(\rho)$ ; (e) the predicted variance of  $\ln(\rho)$  for an ensemble of tomograms, normalized by the variance of true resistivity; and (f) the predicted correlation coefficient between true and estimated  $\ln(\rho)$ .

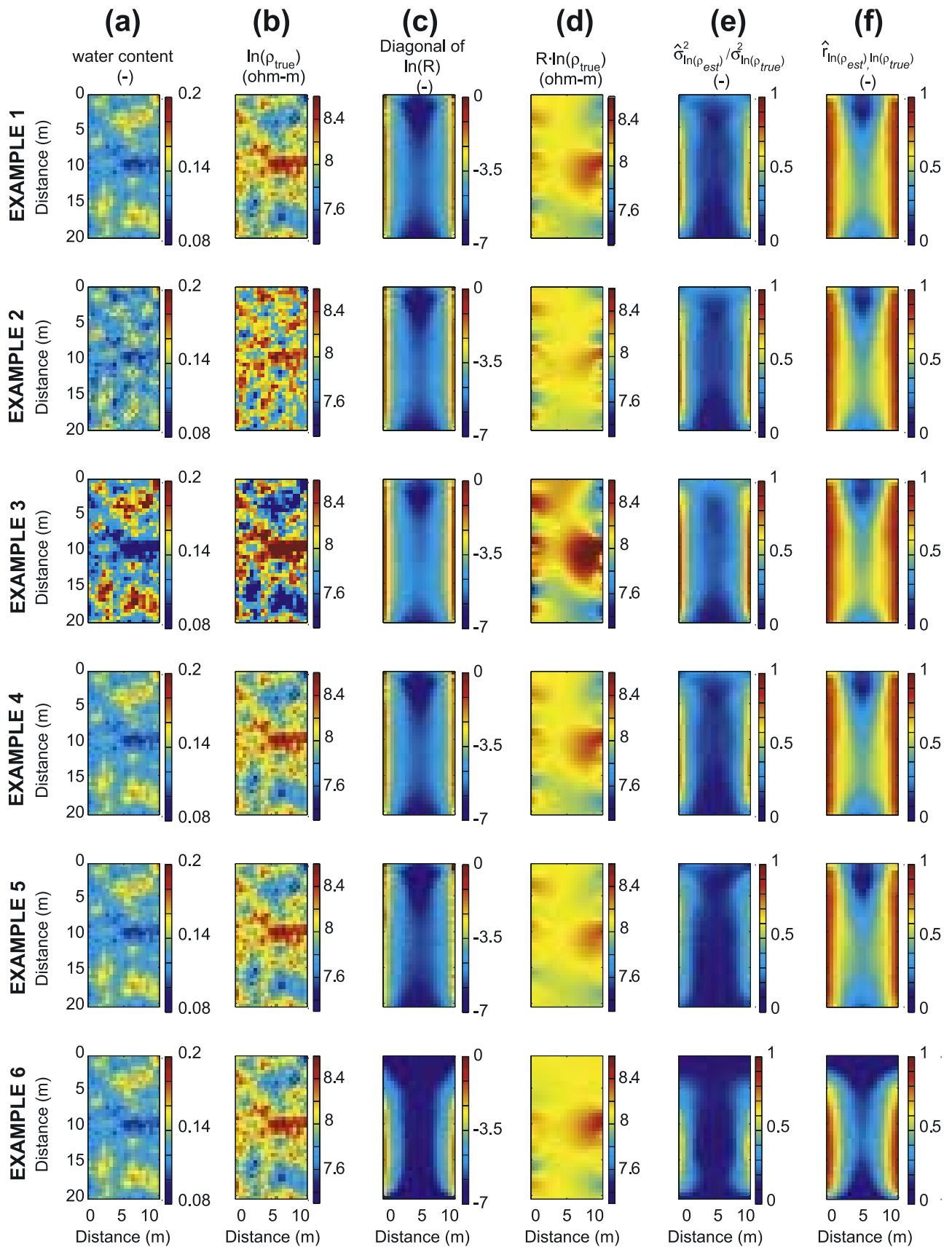


Figure 4

### 3.2.6. Example 6: Effect of Survey Geometry—In-Well Dipoles Only

[51] A common ERT survey geometry is the dipole-dipole survey, where the poles of the current dipole are in the same well, as are the poles of the potential dipole. Considering a geometry comprising only 672 dipole-dipole measurements, there are marked changes in the inversion from example 5, which includes the same number of measurements but a mixed geometry with dipoles split between wells (Figure 4d, example 6). Moreover, the resolution and variance are significantly lower in the center of plane (Figures 4c and 4e, example 6). In areas of low resolution, there will be a correspondingly poorer correlation between geophysical and hydrologic parameters (Figure 4f, example 6). From these results, we conclude that using split dipoles is important for producing high-resolution tomograms.

## 4. Probabilistic, Pixel-Specific, Petrophysical Relations

[52] The series of synthetic examples demonstrates that resolution-dependent correlation loss varies spatially over a tomogram as a function of measurement physics, survey design, regularization, and the magnitude and length-scale of heterogeneity. In this section, we evaluate the implications of correlation loss for application of petrophysical models to convert tomograms of geophysical properties into estimates of hydrologic parameters. Using equations (21)–(23), we construct bivariate probability distribution functions (PDFs) between tomographic estimates and true water content for selected pixels; these PDFs define probabilistic, pixel-specific, petrophysical relations based on the model resolution matrix for a single tomographic inversion. Comparison of bivariate PDFs for selected pixels provides insight into the spatial variability of correlation loss and the applicability of petrophysical relations to tomographic estimates. Comparison of PDFs for ERT and RTT examples provides insight into the effects of physics on the utility of tomograms for quantitative estimation of water content.

[53] The radar-travel time and electrical-resistivity, pixel-specific relations for example 1 (Figures 5 and 6, respectively) illustrate the pattern of spatially variable correlation loss. At pixels where the ensemble variance of estimates is low and/or the correlation between the true and estimated geophysical parameter is weak, the petrophysical relation (*Topp et al.* [1980] or *Archie* [1942]) deteriorates. For the RTT example 1, Figure 5 shows bivariate PDFs of true water content and estimated velocity at selected pixels in the image plane. Correlation loss is evident at pixels adjacent to the borehole (Figures 5d, 5f, and 5h) and in regions where ray density or angular coverage are poor, such as at the top middle (Figure 5e) and bottom middle of the tomogram; at these pixels, high-valued anomalies are strongly underestimated and low-valued anomalies are strongly overestimated compared to the true petrophysical relation, shown as a solid line. Conversely, at well-resolved pixels (Figures 5g and 5i), the bivariate PDFs better reflect the underlying petrophysical relation.

[54] Whereas the measurement physics of RTT is based on EM wave propagation, the ERT measurement physics is

based on diffusive flow; hence the resolving powers of the two methods are expected to differ. In the RTT examples, resolution was good in the middle of the interwell region (Figure 5a), where the largest number of independent measurements is available. By contrast, resolution for ERT (Figure 6a) is weak in the center of the tomogram because the current density decreases away from the electrodes. Consequently, the ERT bivariate histograms for example 1 (Figure 6) show that the relation between estimated resistivity and true water content closely approximates Archie's law at pixels near boreholes (Figures 6f and 6h); however, in areas of low sensitivity, such as the center of the ERT tomogram or above the electrodes, the relation breaks down (Figures 6e, 6g, and 6i), and estimates of  $\ln(\rho)$  provide little information about water content. Application of Archie's law to tomographic estimates in the middle of the tomogram would yield unreliable estimates of water content biased strongly toward the mean value. Comparison of bivariate PDFs for RTT and ERT indicates that correlation loss is more heterogeneous for ERT.

[55] A useful method to summarize the bivariate PDFs is with plots of the expected value of the estimated geophysical property as a function of true water content; this relation can be thought of as the expected apparent petrophysical relation. We determine the expected value for the geophysical estimate by finding the centroid of the marginal (1d) PDF at each value of water content. The expected apparent petrophysical relations are shown as dashed lines in Figures 5 and 6; for comparison, the true underlying petrophysical relation is shown as a solid line. Discrepancies between the two lines indicate bias in converting tomographic estimates to estimates of water content. The two relations are similar in well resolved regions of the tomogram but deviate in poorly resolved areas. For example, conversion of velocity estimates to estimates of water content using the work of *Topp et al.* [1980] would tend to underestimate water content in regions of low velocity and overestimate water content in regions of high velocity, with the degree of bias varying spatially as a function of resolution. The bias could be further studied and quantified by fitting linear or polynomial functions to the curves or the residuals between them.

[56] In addition to upscaled pixel-specific petrophysical relations, random field averaging can be used to construct a global bivariate PDF between tomographic estimates and the related hydrologic parameters. Figure 5j shows the bivariate PDF taken over all pixels in the RTT tomogram, predicted using random field averaging; Figure 5k shows the same plot calculated by comparing true water content and estimated velocity for all pixels in 200 pairs of tomograms and the unconditional realizations upon which the tomograms are based. Comparison of the two plots provides a check on the RFA-based results, which are based on the resolution matrix for a single realization. The RFA results are similar to the numerically derived results, which involve far more computational effort. Figures 6j and 6k show a similar comparison of bivariate PDFs based on the ERT results. The PDFs for RTT and ERT are similar and reveal the same level of error in tomographic estimates of moisture content. The analysis of bivariate PDFs for the ERT tomograms, however, clearly shows

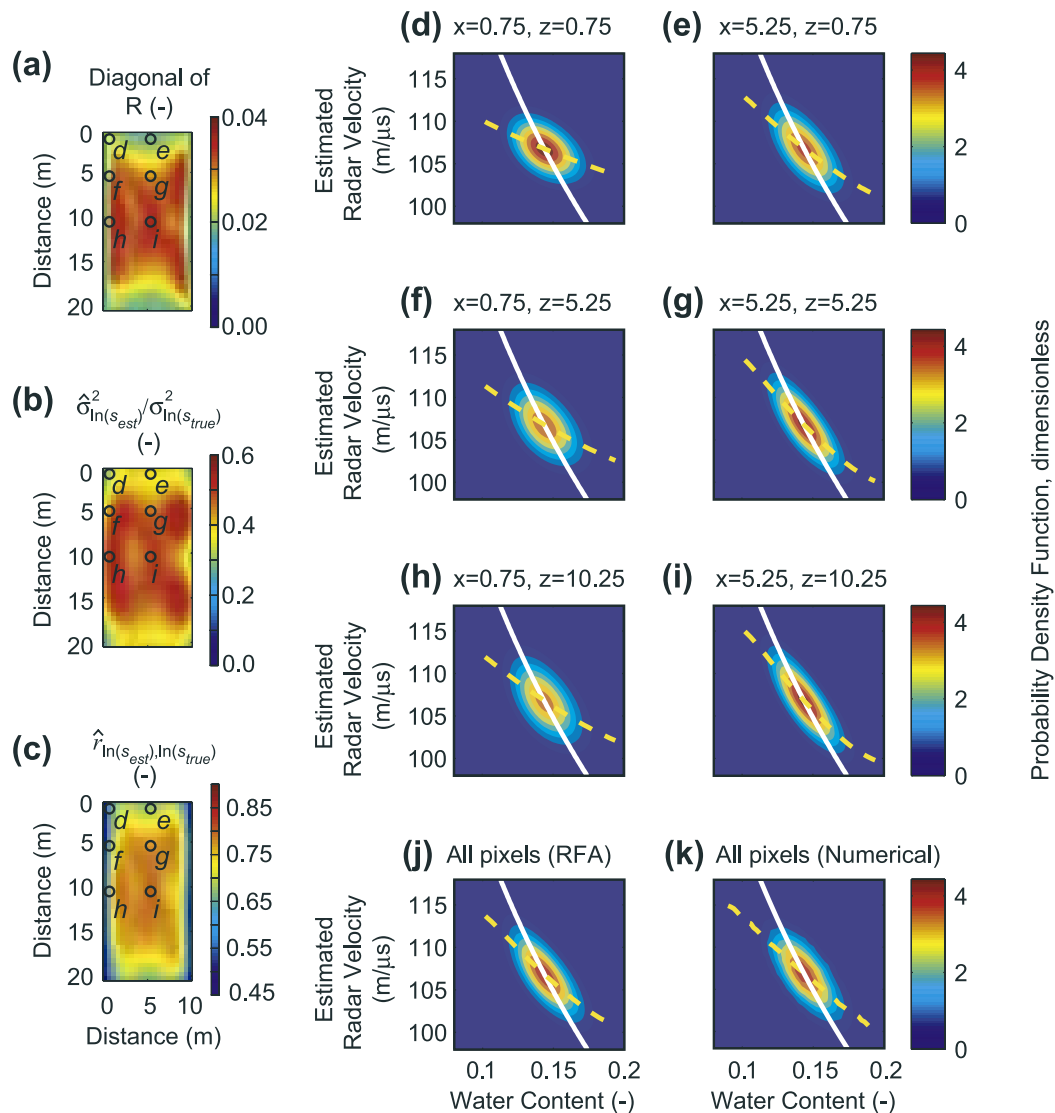


**Figure 5.** Probabilistic, pixel-specific, petrophysical relations for the radar base case. (a) Diagonal of the model resolution matrix; (b) predicted ensemble variance of tomographic estimates; (c) predicted correlation coefficient between estimated and true  $\ln(\text{slowness})$ ; (d)–(i) predicted bivariate probability distribution functions (PDFs) of estimated radar velocity and true water content for selected pixels; (j) predicted bivariate PDF for all pixels in the interwell region; (k) calculated bivariate PDF for all pixels in the interwell region based on comparison of 200 realization-tomogram pairs. In Figures 5d–5k, solid lines indicate the Topp equation relating water content and velocity [Topp *et al.*, 1980]; dashed lines indicate the calculated expected value of estimated velocity as a function of true water content. Circles in Figures 5a–5c indicate locations of pixels for PDFs shown in Figures 5d–5i.

greater pixel-to-pixel variability in comparison to those from RTT.

## 5. Discussion and Conclusions

[57] In this work, we presented analytical methods that allow modeling of resolution-dependent correlation loss as a function of (1) measurement physics, (2) survey geometry, (3) measurement error, (4) the spatial structure of the subsurface, and (5) regularization. The approach provides a framework to evaluate the utility of tomograms for quantitative hydrologic estimation prior to field studies. Examples for both electrical resistivity and radar travel time

tomography provide insights into the roles of measurement physics on the patterns of correlation loss. Although tomograms for most examples recover large-scale structure, the magnitude of anomalies is blunted, the extent of anomalies is overestimated, and the relation between geophysical estimates and true water content may only weakly reflect the true petrophysical relations. In general, ERT performs better near boreholes, whereas RTT performs better in the interwell region; hence the two tomographic modes may provide complementary information for joint inversion and subsequent hydrologic parameter estimation.

[58] We demonstrated an approach to construct probabilistic, pixel-specific, petrophysical relations, i.e., bivariate

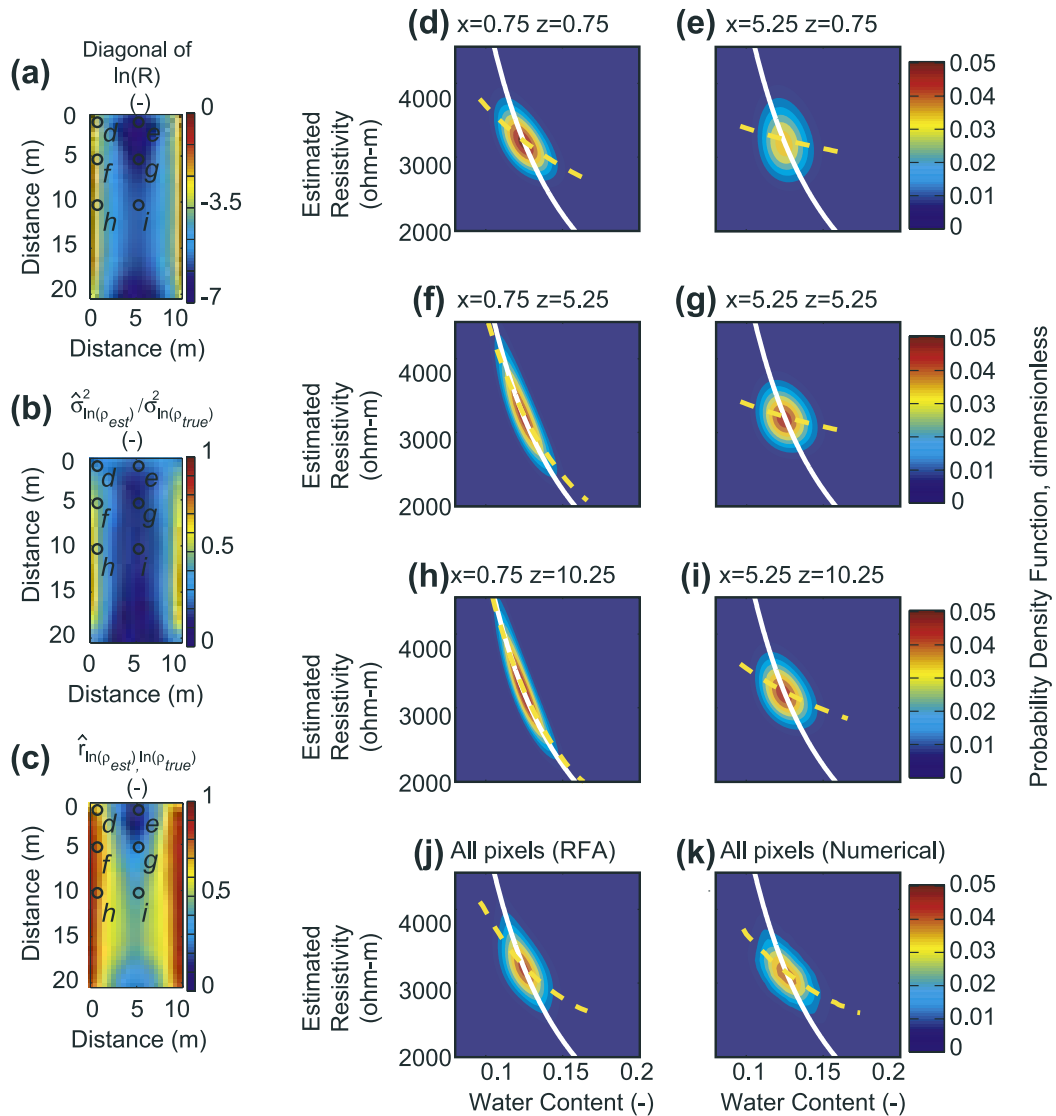


**Figure 6.** Probabilistic, pixel-specific, petrophysical relations for the electrical-resistivity tomography base case. (a) The natural logarithm of elements on the diagonal of the model resolution matrix; (b) predicted ensemble variance of tomographic estimates; (c) predicted correlation coefficient between estimated and true  $\ln(\rho)$ ; (d)–(i) predicted bivariate probability distribution function (PDFs) of estimated resistivity and true water content for selected pixels; (j) predicted bivariate PDF for all pixels in the interwell region; (k) calculated bivariate PDF for all pixels in the interwell region based on comparison of 200 realization-tomogram pairs. In Figures 6d–6k, solid lines indicate Archie's law [Archie, 1942] relating water content and resistivity; dashed lines indicate the calculated expected value of estimated resistivity as a function of true water content. Circles in Figures 6a–6c indicate locations of pixels for PDFs shown in Figures 6d–6i.

PDFs between hydrologic parameters and tomographic estimates of geophysical properties. Our results indicate that application of petrophysical models (e.g., Archie's law and the Topp equation) to tomograms may yield misleading estimates of hydrologic parameters (e.g., water content) for many practical field examples. Tomographic estimates may poorly approximate point-scale measurements; rather, they represent upscaled, local averages. Where tomographic resolution is poor, tomographic estimates revert to the mean value, and hydrologic estimates will be biased. In many applications, reliable hydrologic

estimation based on geophysical tomograms will require consideration of spatially variable, resolution-dependent correlation loss.

[59] In addition to providing insights for designing geotomographic experiments and assessing the utility of tomograms for geostatistical and petrophysical estimation, the pixel-specific relations developed with our approach could be used to improve quantitative interpretation of tomograms. We upscale petrophysical relations to produce pixel-specific, bivariate PDFs between geophysical estimates and the related hydrologic or reservoir property of interest;

these PDFs could be used within Bayesian or geostatistical frameworks to account for spatially variable correlation loss. Alternatively, the PDFs could be used to construct pixel-specific calibrations between the true and estimated geophysical property in an effort to undo the variable blunting and smoothing inherent in tomographic estimates. This would provide a simple, though less rigorous, alternative to the recently proposed full inverse stochastic calibration [Singha and Moyses, 2004; Moyses et al., 2005]. The approach presented here is based on random field averaging and the model resolution matrix, whereas full inverse stochastic calibration determines pixel-specific calibrations using a computationally intensive, numerical procedure involving geostatistical simulation of correlated realizations of geophysical and hydrologic properties; numerical simulation of the geophysical measurements; inversion of the predicted geophysical data; and comparison of the geophysical estimates with the original hydrologic property values for a large number of realizations.

[60] The goals of our work are (1) to raise awareness of the limitations of geophysical tomography for hydrologic estimation; (2) to provide a framework to improve survey design and assess tomograms for hydrologic estimation; and (3) to develop insights into the different patterns of correlation loss for electrical resistivity and radar tomography. The specific examples presented in this paper are based on problems of interest to the environmental and engineering communities; however, our approach has application to, and our results have implications for, other problems in static or time lapse geotomography where a quantitative understanding of the earth is required.

## Appendix A: PDF Transformation

[61] Our approach to developing pixel-specific petrophysical relations requires a method to convert the probability distribution function (PDF) of one property,  $X$ , to that of another property,  $Y$ , given a petrophysical model,  $\Psi$ , such that  $y = \Psi(x)$ . For simplicity, we assume here a petrophysical model where  $y$  increases monotonically with  $x$ , but the method can be adapted for inverse and more complicated relations. For a given PDF of  $X$ ,  $f_X$ , we seek to determine,  $f_Y$ , the PDF of  $Y$ . Consider the cumulative distribution functions (CDFs) of the two properties,  $F_X$  and  $F_Y$ , respectively. As shown graphically in Figure A1,

$$F_X(x_i) = F_Y(y_i) \quad (\text{A1})$$

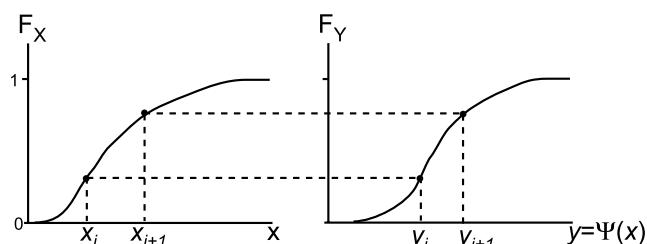


**Figure A1.** Schematic illustrating how the petrophysical relation,  $X$ , relates the cumulative distribution functions,  $F_X$  and  $F_Y$ , of properties  $X$  and  $Y$ .

for all  $i$ . The PDFs are, of course, are the derivatives of the CDFs; for a discretized distribution of  $X$ , we use a difference approximation to relate the CDF and PDF:

$$f_X(x_i) = \left. \frac{dF_X}{dx} \right|_{x_i} \approx \frac{\Delta F_X}{\Delta x} = \frac{F(x_{i+1}) - F(x_i)}{x_{i+1} - x_i} \quad (\text{A2})$$

$$f_Y(y_i) = \left. \frac{dF_Y}{dy} \right|_{y_i} \approx \frac{\Delta F_Y}{\Delta y} = \frac{F(y_{i+1}) - F(y_i)}{y_{i+1} - y_i}. \quad (\text{A3})$$

Given (A1),  $\Delta F_X(x_i) = \Delta F_Y(y_i)$ , and thus

$$f_Y(y_i) \approx f_X(x_i) \frac{\Delta x}{\Delta y} = f_X(x_i) \frac{x_{i+1} - x_i}{\Psi(x_{i+1}) - \Psi(x_i)}. \quad (\text{A4})$$

Equation (A4) amounts to a rescaling of the PDF that results from the difference of units between properties  $X$  and  $Y$ .

[62] **Acknowledgments.** The material in this paper is based on work supported by the U.S. Geological Survey Toxic Substances Hydrology and Groundwater Resources Programs and by the National Science Foundation under grant EAR-0124262. Any opinions, findings, and conclusions or recommendations expressed in this material are those of the author(s) and do not necessarily reflect the views of the National Science Foundation. We are grateful to Geoff Moret of the Pennsylvania State University for providing a Matlab eikonal solver based on a FORTRAN code by David Aldridge of Los Alamos National Laboratory. This manuscript benefited from suggestions by John W. Lane Jr., William F. Waite, Alison Waxman, two anonymous reviewers, and Associate Editor Doug Schmitt.

## References

- Aki, J., A. Christofferson, and E. S. Husbye (1977), Determination of three-dimensional seismic structure of the lithosphere, *J. Geophys. Res.*, **82**, 277–296.
- Alumbaugh, D. L., and G. A. Newman (2000), Image appraisal for 2-D and 3-D electromagnetic inversion, *Geophysics*, **65**, 1455–1467.
- Alumbaugh, D., P. Y. Chang, L. Paprocki, J. R. Brainard, R. J. Glass, and C. A. Rautman (2002), Estimating moisture contents in the vadose zone using cross-borehole ground penetrating radar: A study of accuracy and repeatability, *Water Resour. Res.*, **38**(12), 1309, doi:10.1029/2001WR000754.
- Archie, G. E. (1942), The electrical resistivity log as an aid in determining some reservoir characteristics, *Trans. Am. Inst. Min. Metall. Pet. Eng.*, **146**, 54–62.
- Backus, G., and F. Gilbert (1968), The resolving power of gross earth data, *Geophys. J. R. Astron. Soc.*, **16**, 169–205.
- Berthold, S., L. R. Bentley, and M. Hayashi (2004), Integrated hydrogeological and geophysical study of depression-focused groundwater recharge in the Canadian prairies, *Water Resour. Res.*, **40**, W06505, doi:10.1029/2003WR002982.
- Binley, A., and A. Kemna (2005), DC resistivity and induced polarization methods, in *Hydrogeophysics*, *Water Sci. Technol. Libr.*, vol. 50, edited by Y. Rubin and S. S. Hubbard, pp. 129–156, Springer, New York.
- Binley, A., P. Winship, R. Middleton, M. Pokar, and J. West (2001), High resolution characterization of vadose zone dynamics using cross-borehole radar, *Water Resour. Res.*, **37**, 2639–2652.
- Binley, A., G. Cassiani, R. Middleton, and P. Winship (2002), Vadose zone model parameterisation using cross-borehole radar and resistivity imaging, *J. Hydrol.*, **267**(3–4), 147–159.
- Birchak, J. R., C. G. Gardner, J. E. Hipp, and J. M. Victor (1974), High dielectric constant microwave probes for sensing soil moisture, *Proc. IEEE*, **62**, 93–98.
- Bregman, N. D., P. A. Hurley, and G. F. West (1989), Seismic tomography at a fire-flood site, *Geophysics*, **54**, 1082–1090.
- Cassiani, G., G. Böhm, A. Vesnaver, and R. Nicolich (1998), A geostatistical framework for incorporating seismic tomography auxiliary data into hydraulic conductivity estimation, *J. Hydrol.*, **206**(1–2), 58–74.
- Cerveny, V. (1984), The application of ray tracing to the propagation of shear waves in complex media, in *Handbook of Geophysical Exploration: Seismic Exploration*, vol. 15A, edited by K. Helbig and S. Treitel, pp. 1–124, Geophys. Press, London.

- Dahlen, F. A. (2004), Resolution limit of travelt ime tomography, *Geophys. J. Int.*, *157*, 315–331, doi:10.1111/j.1365-246X.2004.02214.x.
- Daily, W., and E. Owen (1991), Cross-borehole resistivity tomography, *Geophysics*, *56*, 1228–1235.
- Day-Lewis, F. D., and J. W. Lane Jr. (2004), Assessing the resolution-dependent utility of tomograms for geostatistics, *Geophys. Res. Lett.*, *31*, L07503, doi:10.1029/2004GL019617.
- Day-Lewis, F. D., J. M. Harris, and S. M. Gorelick (2002), Time-lapse inversion of Crosswell radar data, *Geophysics*, *67*, 1740–1752.
- Day-Lewis, F. D., J. W. Lane Jr., J. M. Harris, and S. M. Gorelick (2003), Time-lapse imaging of saline-tracer transport in fractured rock using difference-attenuation radar tomography, *Water Resour. Res.*, *39*(10), 1290, doi:10.1029/2002WR001722.
- Day-Lewis, F. D., J. W. Lane Jr., and S. M. Gorelick (2004), Combined Interpretation of Radar, Hydraulic and Tracer Data from a Fractured-Rock Aquifer, *Hydrogeol. J.*, *13*, doi:10.1007/s10040-004-0372-y.
- Deutsch, C. V., and A. G. Journel (1998), *GSLIB: Geostatistical Software Library and User's Guide*, 369 pp., Oxford Univ. Press, New York.
- Friedel, S. (2003), Resolution, stability, and efficiency of resistivity tomography estimated from a generalized inverse approach, *Geophys. J. Int.*, *153*, 305–316.
- Geselowitz, D. B. (1971), An application of electrocardiographic lead theory to impedance plethysmography, *IEEE Trans. Biomed. Eng.*, *BME-18*, 38–41.
- Hubbard, S. S., J. Chen, J. Peterson, E. L. Majer, K. H. Williams, D. J. Swift, B. Mailloux, and Y. Rubin (2001), Hydrogeological characterization of the South Oyster Bacterial Transport Site using geophysical data, *Water Resour. Res.*, *37*, 2431–2456.
- Husen, S., and E. Kissling (2001), Local earthquake tomography between rays and waves: Fat ray tomography, *Phys. Earth Planet. Inter.*, *123*, 129–149.
- Hyndman, D. W., and S. M. Gorelick (1996), Estimating lithologic and transport properties in three dimensions using seismic and tracer data; the Kesterson Aquifer, *Water Resour. Res.*, *32*, 2659–2670.
- Journel, A. G. (1999), Markov models for cross-covariances, *Math. Geol.*, *31*(8), 955–964.
- Kemna, A. (2000), Tomographic inversion of complex resistivity—Theory and application, Ph.D. thesis, Bochum Univ. Osnabrück, Germany.
- LaBrecque, D. J., M. Miletto, W. Daily, A. Ramirez, and E. Owen (1996), The effects of noise on Occam's inversion of resistivity tomography data, *Geophysics*, *61*, 538–548.
- Lane, J. W., Jr., F. D. Day-Lewis, R. J. Versteeg, and C. C. Casey (2005), Object-based inversion of cross-well radar tomography to monitor injection experiments, *J. Environ. Eng. Geophys.*, *9*(2), 63–77.
- McKenna, S. A., and E. P. Poeter (1995), Field example of data fusion in site characterization, *Water Resour. Res.*, *31*, 3229–3240.
- Menke, W. (1984), The resolving power of cross-borehole tomography, *Geophys. Res. Lett.*, *11*(2), 105–108.
- Moysey, S., K. Singha, and R. Knight (2005), A framework for inferring field-scale rock physics relationships through numerical simulation, *Geophys. Res. Lett.*, *32*, L08304, doi:10.1029/2004GL022152.
- Oldenburg, D. W., and Y. Li (1999), Estimating the depth of investigation in dc resistivity and IP surveys, *Geophysics*, *64*, 403–416.
- Park, S. K. (1998), Fluid migration in the vadose zone from 3-D inversion of resistivity monitoring data, *Geophysics*, *63*, 41–51.
- Peterson, J. E., Jr. (2001), Pre-inversion corrections and analysis of radar tomographic data, *J. Environ. Eng. Geophys.*, *6*, 1–18.
- Ramirez, A., W. Daily, D. LaBrecque, E. Owen, and D. Chesnut (1993), Monitoring an underground steam injection process using electrical resistance tomography, *Water Resour. Res.*, *29*, 73–87.
- Rector, J. W., and J. K. Washbourne (1994), Characterization of resolution and uniqueness in crosswell direct-arrival travelt ime tomography using the Fourier projection slice theorem, *Geophysics*, *59*, 1642–1649.
- Schuster, G. T. (1996), Resolution limits for crosswell migration and travelt ime tomography, *Geophys. J. Int.*, *127*, 427–440.
- Sheng, J., and G. T. Schuster (2003), Finite-frequency resolution limits of wave path travelt ime tomography for smoothly varying velocity models, *Geophys. J. Int.*, *152*, 669–676.
- Singha, K., and S. M. Gorelick (2005), Saline tracer visualized with three-dimensional electrical resistivity tomography: Field-scale spatial moment analysis, *Water Resour. Res.*, *41*, W05023, doi:10.1029/2004WR003460.
- Singha, K., and S. Moysey (2004), Application of a new Monte Carlo approach to calibrating rock physics relationships: examples using electrical resistivity and ground penetrating radar tomography, paper presented at Symposium on the Application of Geophysics to Engineering and Environmental Problems (SAGEEP), Environ. and Eng. Geophys. Soc., Colorado Springs, Colo., 22–26 Feb.
- Slater, L., and A. Binley (2003), Evaluation of permeable reactive barrier (PRB) integrity using electrical imaging methods, *Geophysics*, *68*, 911–921.
- Slater, L., A. Binley, R. Versteeg, G. Cassiani, R. Birken, and S. Sandberg (2002), A 3D ERT study of solute transport in a large experimental tank, *J. Appl. Geophys.*, *49*, 211–229.
- Spetzler, J., and R. Snieder (2004), The Fresnel volume and transmitted waves, *Geophysics*, *69*, 653–663.
- Tarantola, A. (2004), *Inverse Problem Theory and Methods for Model Parameter Estimation*, 342 pp., Soc. for Ind. and Appl. Math., Philadelphia, Pa.
- Topp, G. C., J. L. Davis, and A. P. Annan (1980), Electromagnetic determination of soil water content: Measurements in coaxial transmission lines, *Water Resour. Res.*, *16*, 574–582.
- Tripp, A. C., G. W. Hohmann, and C. M. Swift Jr. (1984), Two-dimensional resistivity inversion, *Geophysics*, *49*, 1708–1717.
- Vanmarcke, R. (1983), *Random Fields: Analysis and Synthesis*, MIT Press, Cambridge, Mass.
- Vasco, D. W., J. E. Peterson, and E. L. Majer (1995), Beyond ray tomography: Wavepaths and Fresnel volumes, *Geophysics*, *60*, 1790–1804.
- Vidale, J. (1988), Finite-difference calculation of travel times, *Bull. Seismol. Soc. Am.*, *78*, 2062–2076.
- Vidale, J. (1990), Finite-difference calculation of travelt imes in three dimensions, *Geophysics*, *55*, 521–526.
- Watanabe, T., T. Matsuoka, and Y. Ashida (1999), Seismic travelt ime tomography using Fresnel volume approach, paper presented at 69th SEG Annual Meeting, Houston, Tex.
- Zandt, G. (1981), Seismic images of the deep structure of the San Andreas fault system, central Coast Ranges, California, *J. Geophys. Res.*, *86*, 5039–5052.

A. M. Binley, Department of Environmental Science, Institute of Environmental and Natural Sciences, Lancaster University, Lancaster LA 4YQ, UK. (a.binley@lancaster.ac.uk)

F. D. Day-Lewis, U.S. Geological Survey, Office of Groundwater, Branch of Geophysics, 11 Sherman Place, Unit 5015, Storrs, CT 06269, USA. (daylewis@usgs.gov)

K. Singha, Department of Geosciences, Pennsylvania State University, 311 Deike Building, University Park PA 16802, USA. (ksingha@psu.edu)